Quantitative SPECT Imaging

14

Michael Ljungberg

Contents

M. Ljungberg
Department of Medical Radiation Physics, Clinical Sciences, Lund, Lund University, SE- 221 85, Lund, Sweden
e-mail: Michael.Ljungberg@med.lu.se

14.1 Introduction

The scintillation camera is essentially a device that measures 2D images of a radionuclide distribution in vivo by detecting emitted photons. Due to the construction of the collimator, events in the image coming from photons emitted at different source depths will be superimposed and the source depth will not be resolved. The solution is to obtain the 3D information by measuring projections in different views around the patient and use a reconstruction algorithm. The method is called Single-Photon Emission Computed Tomography (SPECT). If the activity is not redistributed over the time of measurement then the assumption in any reconstruction method is that there exists one unique activity distribution for which a corresponding photon emission will result in the projections that are acquired by the system. Then the goal of any reconstruction process is to determine this distribution in 3D as accurate as possible.

14.2 Factors Degrading SPECT Imaging

In a reconstruction algorithm, such as the filtered backprojection or iterative MLEM/OSEM methods, the goal is thus to find an activity distribution (described by a set of consecutive 2D tomographic images representing different sections in the object) that matches the measured projection data. However, if the measured data suffers from physical effects, such as photon attenuation in the object or unwanted contribution to the projection data from photons scattered in the patient, then the reconstructed solution will not accurately describe the activity distribution [1]. Photon attenuation can actually result in false positive

M.M. Khalil (ed.), *Basic Sciences of Nuclear Medicine*, DOI: 10.1007/978-3-540-85962-8_14,

indications, especially in nonhomogeneous regions such as the thorax. It is therefore of importance to correct for these effects even if the actual numerical pixel values are of less importance.

The following examples that describe the major SPECT imaging degrading factors have been created by the use of the Monte Carlo program SIMIND [1, 2] and the NCAT anthropomorphic mathematical phantom [3, 4]. The Monte Carlo method allows for a simulation of the photons from emission in an object to the detection in a scintillation camera. During this process, it is possible to keep track of the interaction history of the photons and the formation of the image from these photons. The advantage of categorizing each event in the image based on origin, that is, from primary, scattered, or penetrated photons, is that it makes it possible to study the degradation in detail. Most of the examples in this chapter are based on activity distributions that mimic a myocardial perfusion study. Different photon energies have been simulated for visual purposes, but some of these energies may not be clinically relevant to the simulated radionuclide distribution.

14.2.1 Distance-Dependent Spatial Resolution

The commonly used parallel-hole collimator has the advantage of having a geometrical sensitivity that is independent of source-to-collimator distance of the source within the field of view (FOV). This means that the conversion factor (cps/MBq) remains constant within the FOV, which greatly simplifies the process of activity quantitation. The spatial resolution however depends on the distance to the collimator and the specification of the holes (diameter, shape, septum thickness, and length). In a clinical environment, it is common to have several types of collimators available, selected on the basis of the type of study and the energy of the photon. Examples are low-energy high-resolution (LEHR), low-energy general purpose (LEGP), medium-energy general purpose (MEGP), and high-energy general-purpose (HEGP) collimators. Because of the underlying design, even a parallel-hole LEHR collimator will limit the spatial resolution to be, at the best, about 10–15 mm for SPECT. This means that although the correct number of counts are acquired by the camera, the position of each event are spread out over a large area (more pixels) if the source is located at a larger distance. This effect can be seen in Fig. 14.1, where profiles through images of three-point sources being located at different distances from the collimator surface are shown for both LEGP and LEHR collimators. The profiles show a larger value of the FWHM as the source moves away from the camera. This broadening is less pronounced for the LEHR collimator but with an expense of reduction in measured count rate.

The distance-dependent blurring of an image means that the cps/pixel will not reflect the MBq/ml in a particular voxel. This unwanted effect is often called the partial-volume effect. The spatial resolution also affects the image contrast and hence the ability to detect small lesions with moderate lesion-to-background activity ratios. In principle, however, very small lesions can be detected, but the lesion-to-background activity ratios in these cases need to be very high; however, the volume of a lesion can never be measured below the order of the spatial resolution of the system.

14.2.2 Photon Attenuation

Some of the photons, emitted from a radiopharmaceutical administered to a patient will interact within the patient and therefore not contribute to the image formation in the expected way. The basic interaction types for photon energies that are important to nuclear medicine applications are photoabsorption, Compton scattering, Rayleigh scattering, and pair production (rare since this interaction type can occur only for photons with energies above 1.022 MeV). Consider a fluence of photons impinging in a narrow-beam geometry on an object of the thickness x and the density . The number of photons, N, that pass through the object is given by

$$N = N_0 e^{-\frac{\mu}{\rho}\rho \cdot x} \tag{14.1}$$

where N_0 is the initial narrow-beam photon fluence and N is the photon fluence after passing through the object. The probability of each of the possible interactions can be described by differential attenuation coefficients, and, consequently, the sum of these differential

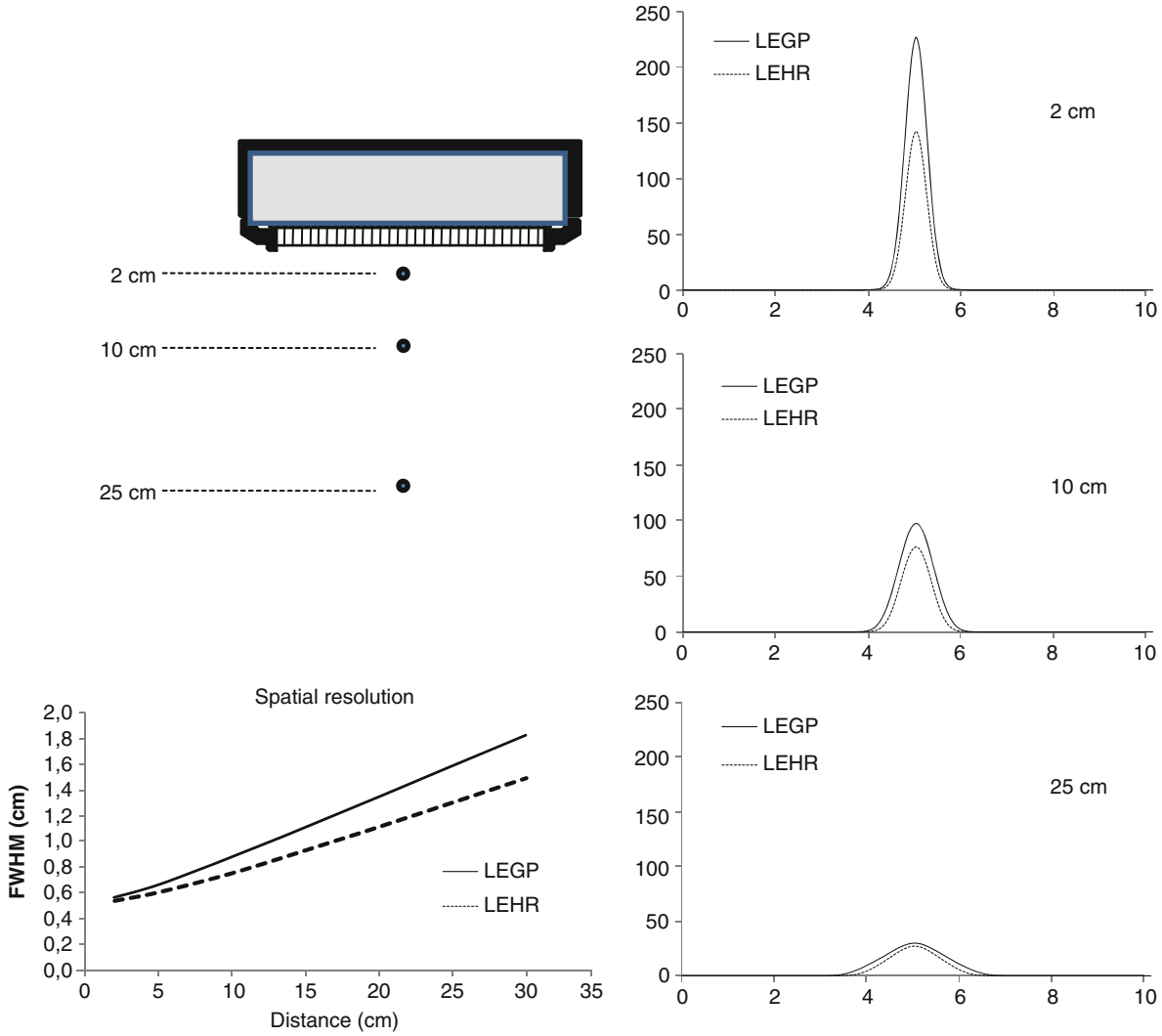

Fig. 14.1 Simulated point-spread function for a point source located at distances 2 cm (**a**), 10 cm, (**b**) and 25 cm (**c**) to the lower collimator surface. The images illustrate the importance of always keeping the camera as close as possible to the patient surface. The figure also shows that the magnitude of the degradation in spatial resolution for the two collimators also differs

coefficients describes the probability for any type of interaction. This sum of coefficients is the *linear* attenuation coefficient .

$$\mu = \tau_{\text{photo}} + \sigma_{\text{inc}} + \sigma_{\text{coh}} + \kappa_{\text{pair}} \tag{14.2}$$

Photon attenuation depends on the photon energy (he), composition (*Z*), and the density () of the object and values are often tabulated as mass-attenuation coefficients, / (Fig. 14.2).

In a photo-absorption event, the energy of a photon is transferred to an electron in the interacting atom. This electron will, if the photon energy is high enough, liberate itself from the atom and leave the atom with a kinetic energy equal to the incoming photon energy minus the binding energy of the electron. When the vacancy in the electron shell is filled from an outer electron, the binding energy is emitted either as a characteristic x-ray photon or as an Auger electron. The probability for these occurrences depends on the atomic number of the material. Auger electron emission dominates for low-Z tissue-equivalent materials.

Figure 14.3 shows four frontal projections (Fig. 14.3a–d) of the NCAT phantom simulated for

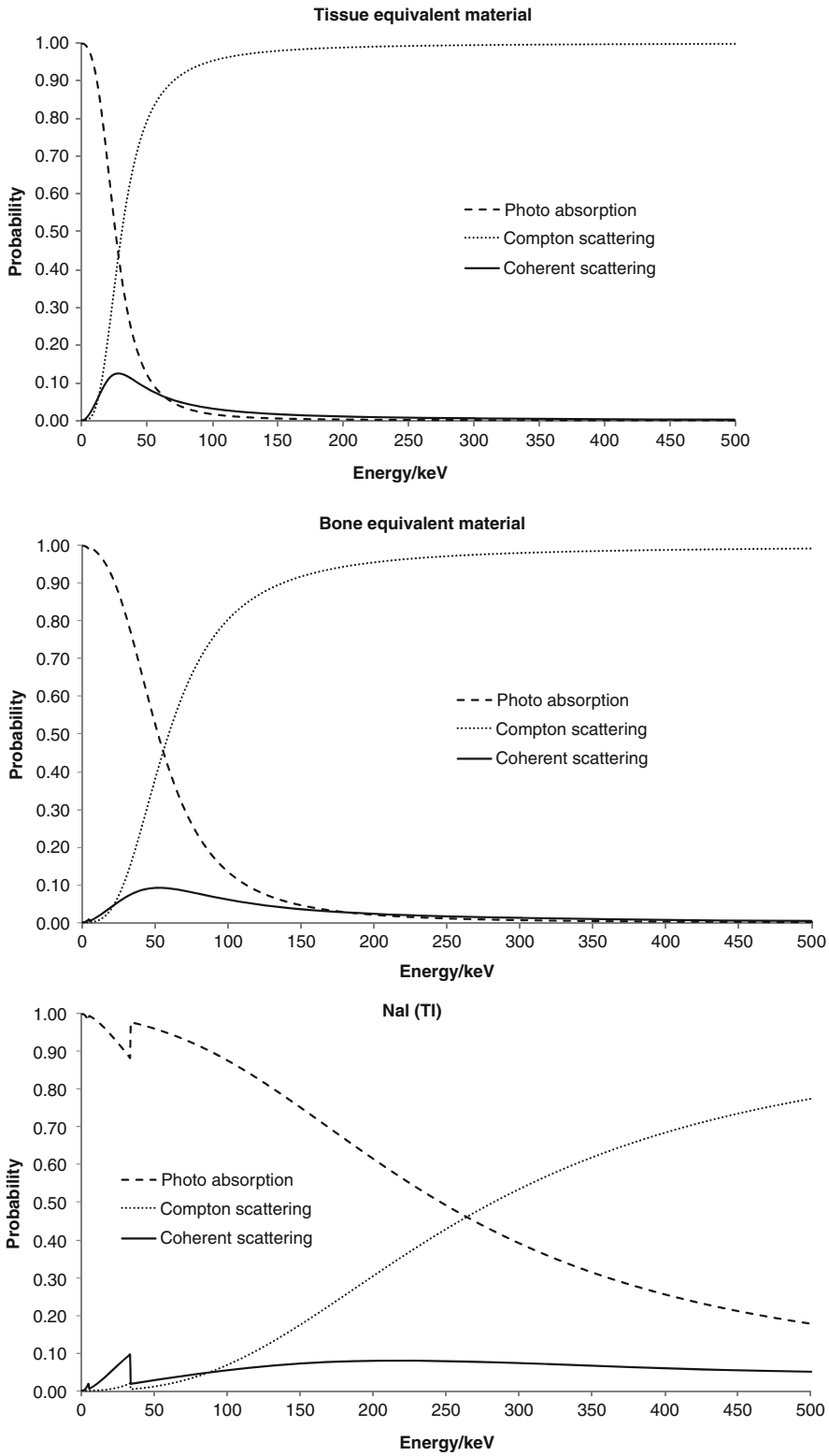

Fig. 14.2 The relative probability for photoabsorptions, Compton scattering, and Rayleigh scatterings in the energy range of 500 keV and lower for tissue-equivalent material (*upper*), bone-equivalent material (*middle*), and for NaI (*lower*). Note the rapid decrease in probability for photoabsorption in tissue. Also note also that these data are relative and that the magnitude of the attenuation is much larger for NaI(Tl) as compared to water

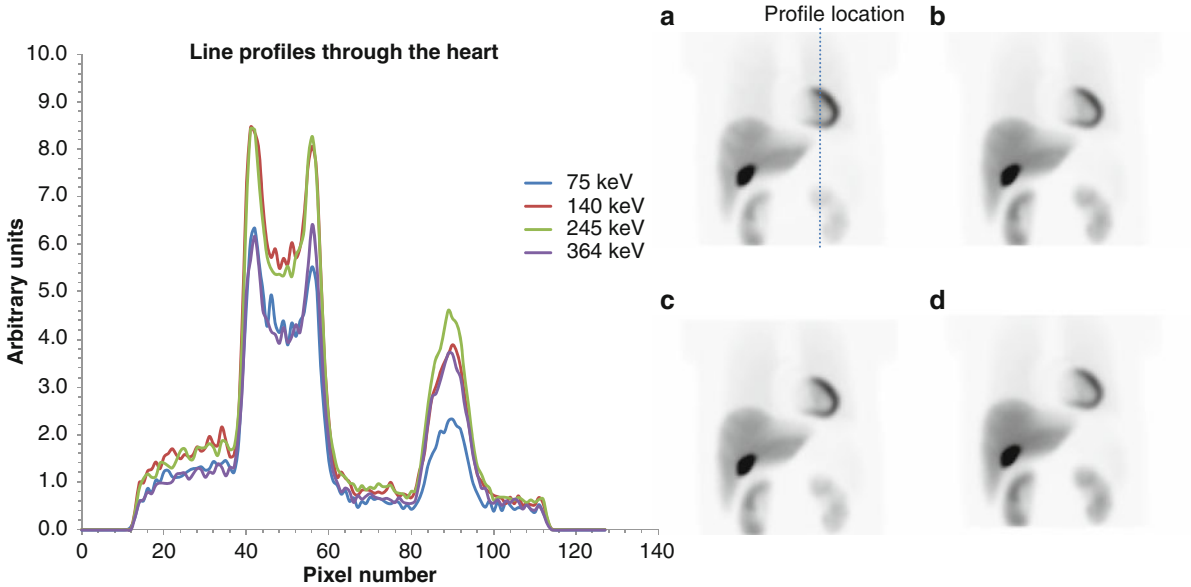

Fig. 14.3 Four frontal projections of the NCAT phantom showing the effect of photon attenuation in the cases of 75 keV (**a**), 140 keV (**b**), 245 keV (**c**), and 364 keV (**d**) photon emission, respectively. Vertical line profiles through the heart and part of the left kidney have been calculated and are compared in the *left diagram*. The *dotted line* in projection A indicates the location of the profiles. Note that imaging 75 keV and 364 keV photons result in about the same count rate. Also, note that these figures were simulated considering "only" photon attenuation

four different photon energies (75, 140, 245, and 364 keV, respectively). The effect of attenuation is shown as a decreased count level in the heart region and especially in the left kidney, a diminished uptake can be seen. The registered count rate also depends on the attenuation in the crystal. Imaging high photon energies that experience less attenuation in the phantom does not always reflect a high count rate because of the increased probability for the photon to travel through the crystal without any interaction and related contribution to the image formation.

14.2.3 Photon Scatter

The problem with photon scatter has its origin in the limitation of the scintillation camera to accurately measure the energy imparted in the NaI(Tl) crystal. The processes of converting the imparted energy to visible light photons and to guide these photons to the photomultipliers to achieve measurable signals are inherently a stochastic procedure. Therefore, the measured signal will have a statistical error even if the imparted energy always remains the same. For new NaI(Tl) crystals, this statistical error is about 8–10% (FWHM) for an absorbed energy of 140 keV. This relatively large error implies that an energy discriminator needs to cover about twice that width (16–20%) in order to maintain a reasonable counting statistics. Some of the photons that have been scattered in the patient with a small deflection angle (small loss of energy) will therefore have a possibility to be detected within such a large energy window and thus contribute to the image formation, but these photons carry wrong spatial information about the decay location in the object. The effect when registering scattered events will result in a degraded image contrast and a potential problem if aiming to quantify regional activity uptakes (Fig. 14.4).

The energy hv´ of a scattered photon is directly related to the deflection angle according to the Compton equation.

$$h\upsilon' = \frac{h\upsilon}{1 + \frac{h\upsilon}{m_o c^2}(1 - \cos\theta)} \tag{14.3}$$

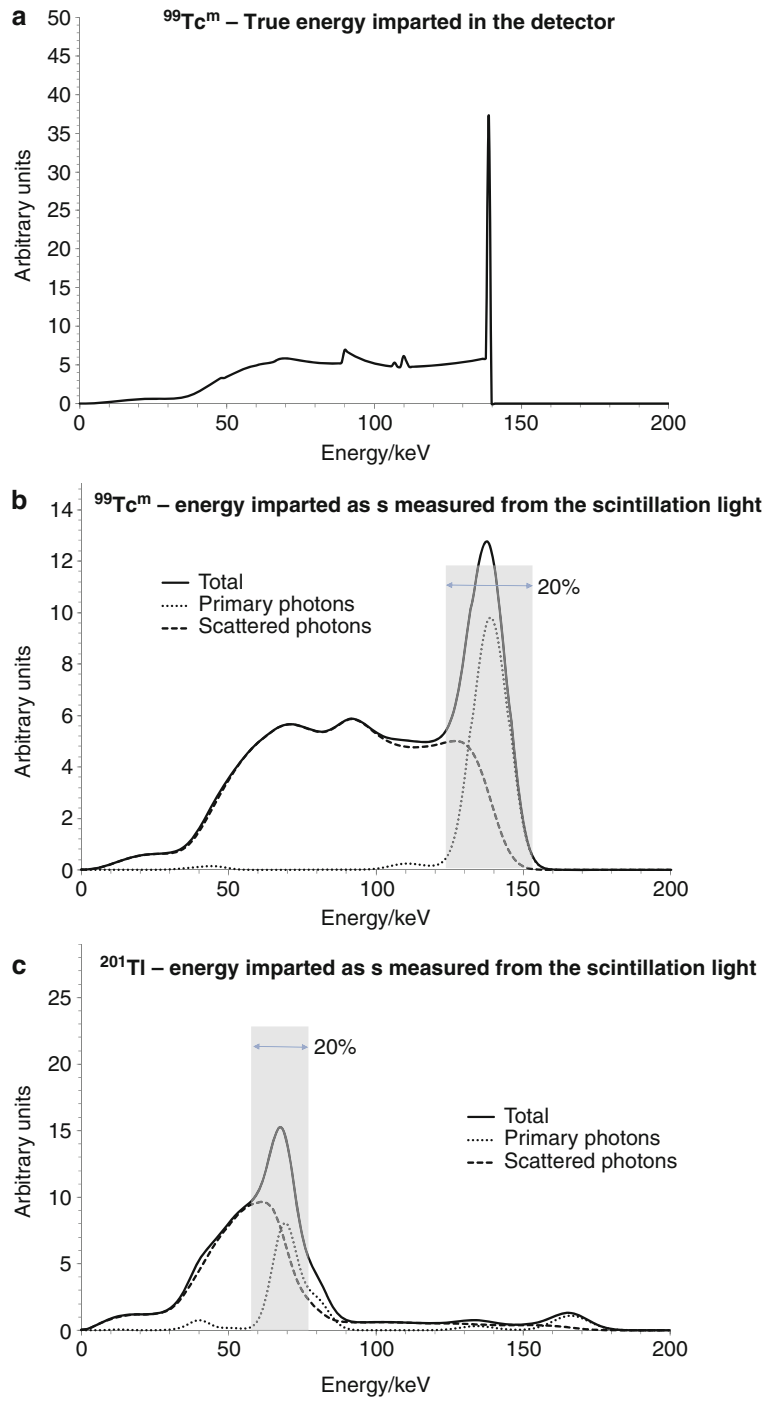

Fig. 14.4 The upper diagram (**a**) shows the true imparted energy in the NaI(Tl) crystal from 140 keV photons. Note the sharp peak that occurs because the full absorption from 140.5 keV photons will be within the same energy channel. The middle diagram (**b**) shows simulated data corresponding to a measured energy spectrum. The peaks have been broader due to the poor energy resolution of the camera. Because of this inaccuracy in the energy measure, some photons that have been scattered in the phantom are detected within the energy window. Diagram (**b**) also display curves that represent events from primary unattenuated photons and events from photons scattered in the object. Note that a substantial fraction of scattered photons will contaminate the images acquired within the energy window. Note that in the acquired image, it is not possible to distinguish these events from the primary events. Diagram (**c**) shows corresponding data for ^{201}Tl

For higher photon energies, the scattering angles tend to peak in the forward directions, but at moderate photon energies (100 keV), the distribution is relatively symmetrical with a slightly lower probability for ±90° scattering angles. The differential cross section, as described by the Klein-Nishina relation

$$\frac{d\sigma}{d\Omega} = \left(\frac{r_o^2}{2}\right)\left(\frac{h\upsilon}{h\upsilon'}\right)^2\left(\frac{h\upsilon}{h\upsilon'} + \frac{h\upsilon'}{h\upsilon} - 1 + \cos^2\theta\right) \quad (14.4)$$

which determined the probability for a photon being scattered by an angle into a solid angle d relative to the incoming photon trajectory. Equation 14.4 has been derived assuming that the electron is not bounded to the nucleus and in rest. When the photon energy decreases, the effect of the binding to the nucleus slightly changes the cross sections.

Since the contribution of scatter in a SPECT projection is a consequence of photon interactions in the object, the amount of scatter (sometimes defined as the scatter-to-total fraction) depends on photon energy, source depth and distribution, and on tissue composition in addition to camera-based parameters, such as, energy resolution and energy window settings. Figure 14.5 shows the dependencies on the scatter-to-total fraction as function of these parameters.

From Fig. 14.5a, it can be seen that the scatter-to-total fraction increases with increasing source depth but levels out at or above moderate source depth (>20 cm). This is because, although scattering increases with depth, the scattered photons will also be more attenuated compared to the primary photons with higher energies. The degradation in image quality, due to Compton scattering, is also a function of the energy resolution (and thus related energy window setting) but, as can be seen from Fig. 14.4b and c, the dependence of these two parameters is very moderate. Thus, even for new crystals, the scatter-to-total fraction in a scintillation camera images remains quite high (30–50%). When reviewing tabulated cross sections for Compton scattering [5], one can see that the relative number of Compton scattering interactions increases with increasing photon energy, as can be seen in Fig. 14.2. It is therefore somewhat contradictory that scatter problem in SPECT is larger for photons of low energies (Fig. 14.4d). The reason for this is that a fixed energy window centered on the photo-peak energy is used. For an initial high photon energy, the relative loss of energy to a secondary electron in a Compton scattering is quite large which results in a scattered photon of significantly lower energy as when compared to using the energy window discriminator in the lower part of the energy distribution. For a lower initial photon energy, the relative loss of energy in a Compton scattering is small which implies that even for a large scattering angle, there is a good chance that a scattered photon in that energy range will be detected within the fixed energy window.

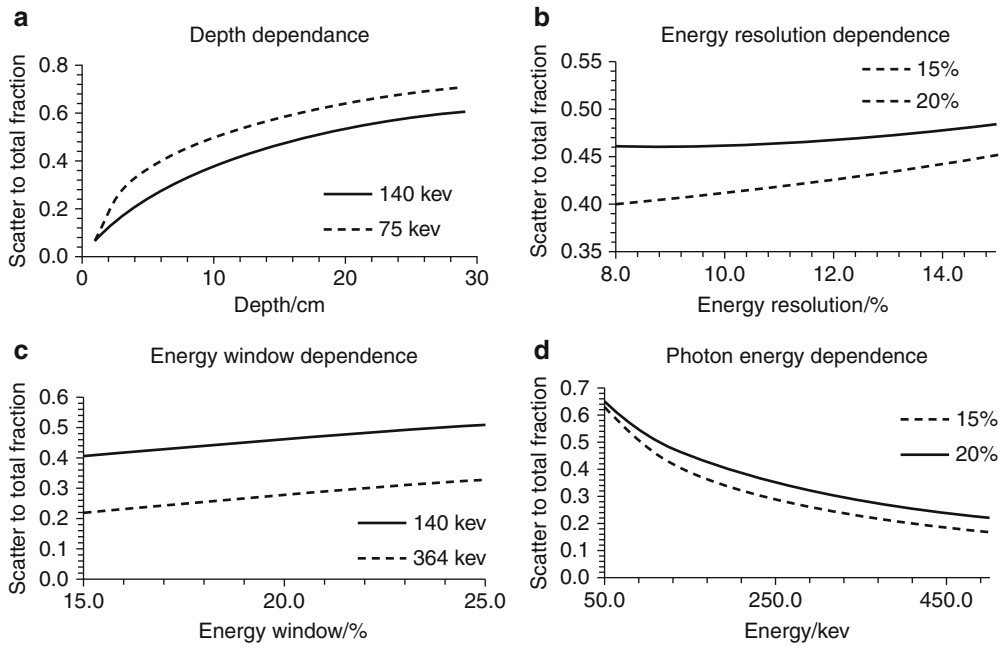

Fig. 14.5 The four diagrams show the scatter-to-total dependence on (**a**) the source depth, (**b**) the energy resolution, (**c**) the energy window setting, and (**d**) the photon energy. Two energy windows of 15% and 20% have been used when appropriate. The data have been simulated using a cylindrical water phantom of 11 cm radius and 20 cm length. The point source is located in center of the phantom for the results in graph (**b–d**)

14.2.4 Collimator Penetration

As mentioned above, the purpose of the collimator is to select only those photons emitted in a direction mainly determined by the axial direction of the collimator hole and to reject all photons emitted in other directions. However, because of the exponential characteristics of the photon attenuation, there will always be a finite probability for a photon to penetrate the collimator walls and thus interact in the crystal further away from the positions defined by the location of the hole. When constructing a collimator, the selection of the thickness of the walls is therefore a compromise between spatial resolution and system sensitivity and the chance for septum penetration.

To illustrate this effect, consider the simulated images shown in Fig. 14.6. Image (a) shows a simulation with 140 keV (^{99m}Tc) and a LEHR collimator and where a good image quality has been obtained. The second image (b) shows a simulation with photons of 364 keV (^{131}I) but still using a LEHR collimator. The image is completely deteriorated due to septum penetration and is, in practice, useless. The third image (c) shows the same simulation with 364 keV photons but now with a HEGP collimator. Because of the thicker septa (1.8 mm instead of 0.2 mm), the penetration effects have been reduced and a useful image quality has been obtained. The last image (Fig. 14.6d) shows a simulation with photon emission from a complete decay of ^{131}I including also the higher photon energies of 637 keV (7.3%) and 723 keV (1.8%). Even though the abundance of these photons is numerically of small magnitudes, the high photon energies make the photons penetrate the walls even when using a HEGP collimator [6] and contribute significantly to the image formation. The degradation in image quality from these high-energy photons can be clearly seen in Fig. 14.6d.

The problem with septum penetration can be reduced by either using a collimator with thicker septa [7] of better attenuating properties, such as tungsten, or the effect can be included in some kind of correction method. If the septum penetration can be modeled, then this effect can be included as a collimator-response function in the forward projection step on an iterative reconstruction method.

14.2.5 Physiologic and Patient Motions

When acquiring data with a SPECT camera, one should always remember that the acquisition is made using a "camera shutter" that is open during the whole acquisition time. This means that if the patient is moving, this will result in degradation in the spatial resolution and in some cases, cause artifacts. Even if the patient is carefully strapped and remains very still, some movements cannot be avoided and these are the respiratory movements and the motion of the heart [8].

The respiratory movements due to breathing make a spatial change that depends on the organ. Since the frequency of the breathing is different as compared to the frequency of the cardiac motion, the respiratory movement will also have an effect on the quality of cardiac imaging even if gated SPECT is applied. The motion is complicated with translations in axial or superior/inferior direction causing a blurred image with a potential reduction of counts in anterior and inferior walls. In tumor detection, the form of the

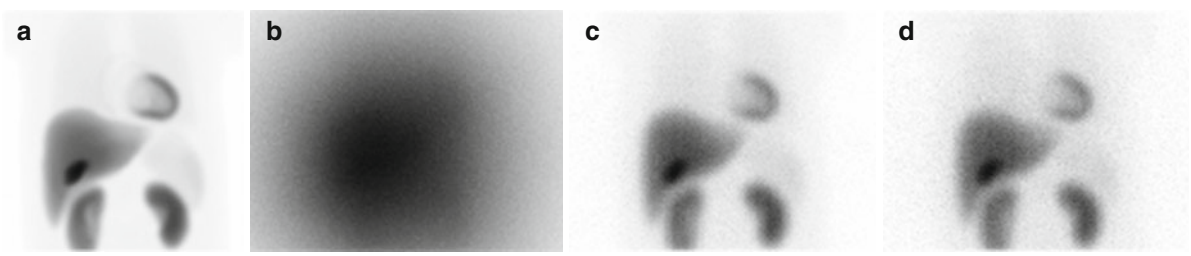

Fig. 14.6 The left image (**a**) shows 140 keV photons impinging on a camera with a LEHR collimator. Next image (**b**) shows 364 keV photons on a camera with the same collimator optimized for 140 keV. Image (**c**) represents an acquisition of 364 keV photons with a dedicated high-energy collimator and image (**d**) is the case where the complete ^{131}I decay has been simulated including also the high-energy photons in the decay

tumor may change to a more elongated or elliptical shape because of breathing and the result is also a lower image contrast. This has been seen in lung studies with PET and ^{18}F-DG.

14.2.6 Image Noise

Because of the randomness of a photon history, an acquired SPECT image will be affected by statistical errors and related image noise. The noise distribution of scintillation camera image follows the Poisson distribution where the variance of a measure in a region-of-interest is the sum of the counts. This implies that in order to get a good image quality, a sufficient long acquisition time together with a high administered activity should be used. The image noise also depends on the selection of matrix size. Changing from 64 64 to 128 128 in matrix size will increase the variance in a projection pixel by a factor of four. Also note that reconstruction is usually made slice by slice which means that the slice thickness (and consequently the acquired number of counts) is half for a 128 128 as compared to a 64 64. The mean counts per voxel in a reconstructed SPECT image will therefore be reduced by a factor of eight. It is thus not always an advantage to increase the matrix size. The time per projection and the number of projections are also of importance. These factors need to be optimized for each study since noise due to improper acquisition parameters can propagate through the reconstruction process and create artifacts in the final image.

14.2.7 Other SPECT Degradation Factors

It is essential that the scintillation camera is well tuned and calibrated. This is especially true for SPECT since deficiencies can result in visible artifacts. For example, nonuniformities in a planar image can be of less importance and sometimes hard to detect, but when reconstructing data from a SPECT camera with nonuniformity regions, artifacts appearing as distinct rings in the image can be seen. The center-of-rotation (COR), that is, the alignment of the electronic center used in the reconstruction algorithm to the mechanic center of the camera orbit is also important to tune. A small error in COR results in degradation of spatial resolution and if larger shift occurs, then ring artifact can appear. It is also important to calibrate the pixel size carefully when performing correction for attenuation and other quantitative measures. A wrong value can result in either under- or overcorrection due to errors in the parameter x in Eqn 1. Other factors that can influence the accuracy in a SPECT study are the selection of acquisition parameters and the noise related to these. The most important selection here is the number of projections and the matrix size. There is a relation between the expected spatial resolution in an image and the number of samples (angles and pixels) as determined by the Nyquist frequency and the number of angular intervals.

Reaching this frequency limit may, in some cases, be difficult depending on the activity administered to the patient and the time required for the acquisition. Generally, there is a trade-off between image quality (the combination of spatial resolution, image contrast, and noise level) and realistic acquisition times and levels of administered activity. Often, image processing including low-pass filtering are required but here, one needs to remember that by using postacquisition image filtering, one sacrifices some extent of the spatial resolution. In some investigations, where high administered activities are used, limitations in the camera's count rate performance can lead to unexpected results. Dead time problems and pulse pile-up effects can change the system sensitivity (cps/MBq) and calibration factors for scatter correction methods, but also significant mis-positioning of events due to unwanted contribution of scintillation light from earlier events may occur, because the position of an event is calculated from the centroid of the emitted scintillation light. In this context, it should be remembered that calibrations made for low-count rates might thus not be relevant in high-count rate imaging.

Since data is collected for a relatively long time interval, it is important that the patient remains at the same position. Some movements such as cardiac motion and breathing can, however, not be avoided. Accounting for cardiac motion can be made by gated SPECT where the cardiac cycle is divided into a number of separate time-frame acquisitions based on the ECG information and especially the R-R interval. It has been a standard procedure for many years to

collect information by this technique and display separately reconstructed images of the different time intervals in a cine-mode display. The factor that hampers the image quality the most is noise because of the limited amount of collected count for 8 or 6 frame gated SPECT. Spatial and temporal filtering is a prerequisite here for a reasonable image quality. In addition, often the number of projections and the number of time frames per cardiac cycle is reduced in order to increase time per projection for a given total acquisition time.

As a summary of this subsection, Fig. 14.7 shows how the image is degraded by the different factors discussed above. The upper row is the frontal projections and the lower is corresponding reconstructed transversal image selected at a location through the heart. Reconstructions were made with an iterative OSEM algorithm without any corrections. Simulation was made using 64 angle projections and a 360-degree rotation mode. The matrix size was 128 128 and 6 iterations and 16 subsets were used in the reconstruction. The first set of images (a) represents no motion of the heart and breathing and an acquisition with a perfect system. Note that the reconstructed image still shows some degradation in spatial resolution due to the finite sampling in projection angles, matrix size, and of the forward projection algorithm. The second column (b) shows the blurring due to respiration and heart motion. When determining the expected image quality reachable in clinical studies based on phantom experiments, it is important to keep this motion in mind since physical phantoms are most often static. In addition, the third column (c) includes degradation in the spatial resolution caused by the characteristics

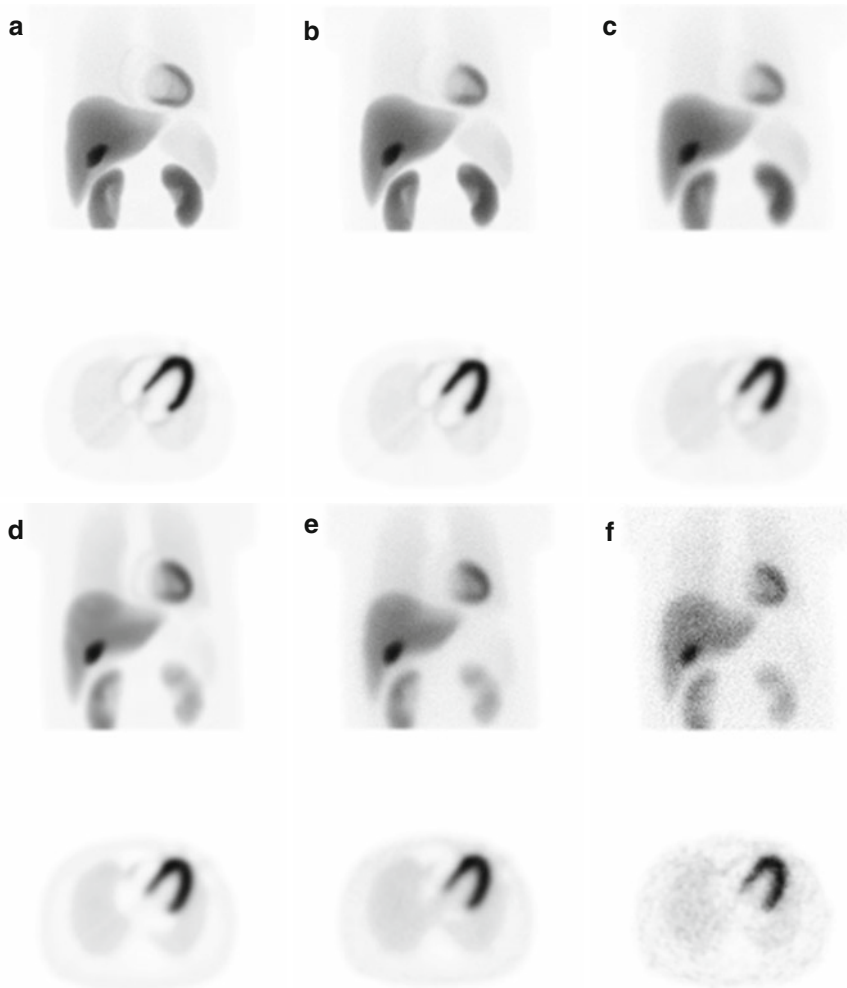

Fig. 14.7 Column (**a**) corresponds to an imaging situation without patient motion and a perfect camera resolution. Next column (**b**) includes patient movements (respiration and heart beating). Column (**c**) represents an image with a typical system resolution and patient movements. Column (**d**) also includes photon attenuation. Column (**e**) includes photon attenuation and scatter contribution and column (**f**) is the same as column (**e**) but with a realistic noise level added

of the LEHR collimator. The forth column (d) includes attenuation of primary photons but no scatter contribution. This mimics a system with perfect energy resolution and a corresponding narrow energy window. The fifth column (e) also includes the presence of scatter due to the limited energy resolutions. The last column (f) has the same images as in column (e) but with a realistic noise level added.

14.3 Correction Algorithms

The objective of a reconstruction method is to obtain a source distribution, described as transversal images, that matches the measured projections as accurate as possible. However, if the measured data are affected by photon attenuation, scatter, and collimator blurring the reconstructed images will be more or less wrong. It is therefore important that these physical effects are compensated for even if the numerical values in the final image are of less importance in order to obtain a diagnostic high-quality image with better sensitivity and specificity.

14.3.1 Attenuation Correction Methods

When using filtered backprojection (FBP) method to reconstruct images, an attenuation correction needs to be applied either prior to the reconstruction step or after. As a preprocessing method, the conjugate-view method can be applied if opposite projection data are available. The main advantage is that the source depth dependence x in Equation 14.1 is cancelled out when combining opposite projections by a geometrical-mean operator on a pixel-by-pixel basis. Let p_{ant} and P_{post} be the counts in opposite projections and P_{air} the counts registered in both cameras without attenuation (assuming a parallel-hole collimator with invariant system sensitivity within the FOV). Then the geometrical mean is calculated from

$$\begin{aligned}\sqrt{P_{\text{ant}} \cdot P_{\text{post}}} &= \sqrt{P_{\text{air}}\ \mathrm{e}^{-\mu d} \cdot P_{\text{air}}\ \mathrm{e}^{-\mu(T-d)}} \\ &= \sqrt{P_{\text{air}}^2 \cdot \mathrm{e}^{-\mu T}} = P_{\text{air}} \cdot \mathrm{e}^{-\mu T/2} \end{aligned} \quad (14.5)$$

where d is the distance from the source to the surface along the projection line toward detector A and T is the total thickness of the patient along the same projection line. The equation is valid only for point-like sources and uniform attenuation. Still, this method is used frequently in planar imaging activity quantitation.

The Chang method [9] is a postprocessing method that is applied on reconstructed SPECT images. The base for this method is the calculation on an attenuation factor averaged for all angles and determined for each voxel location within the boundary of the object. The method can be mathematically described as

$$AF_{i,j} = \frac{1}{N}\sum_{\theta} AF_{i,j,\theta} \quad \text{where} \quad AF_{i,j,\theta} = e^{\sum i,j,\theta\ \mu\Delta x} \quad (14.6)$$

If information about heterogeneous attenuation, expressed as a map of varying values, can be obtained by some type of transmission study (see more about this below), then this information can be included in the calculation of the attenuation factor. The Chang compensation method can be found on commercially available systems and has been successful in situations where the attenuation distribution is relatively uniform. The method may result in imperfect attenuation compensation and has inferior noise properties.

Today, the most frequently used compensation method for attenuation is as part of an iterative reconstruction method. A common feature of all iterative reconstruction methods is the calculated projection obtained by forward projecting a first-guess estimation of an activity distribution into the projection space. By comparing these calculated projections to matched measured projections using some kind of cost function, the need for an improvement (often denoted "an update") of the initial estimated activity distribution can be determined. Photon attenuation is implemented in the forward projection step before calculating the final projection bin. Information about nonuniform attenuation distribution can be included in the projection step if appropriate attenuation maps are available through transmission scans or registered CT images.

14.3.2 Measurement of Photon Attenuation

Properly correcting for attenuation in the thorax region requires a measurement of the distribution of attenuating tissue (an attenuation map) from a

transmission measurement using an external radiation source mounted on the opposite side of the patient. Two measurements are required; one with the patient in site and one blank study. By calculating the quota between the two projections on a pixel-by-pixel basis, line integrals of the attenuation coefficients can be calculated from the following formula

$$\sum \mu_i = \frac{1}{\Delta x} ln\left(\frac{P_{\text{patient}}}{P_{\text{blank}}}\right) \qquad (14.7)$$

where x is the pixel size. These -projections can then be reconstructed using either filtered backprojection or by using iterative reconstruction methods. If a radionuclide is used as a radiation source, it is generally desired to have properties so that the transmission scan can be made simultaneously to the emission scan. This implies that the radionuclide needs to be different from the main radionuclide in order to separate transmission data and have a high activity. The most commonly used radionuclide in commercial systems has been ^{153}Gd with a half-life of 242 days and two major photon energies of 97.5 keV (29.5%) and 103 keV (21.1%), respectively. The method with a radionuclide source suffers from several limitations. First, photons emitted from the main radionuclide (often ^{99m}Tc) that are scattered in the patient can be registered in the lower transmission energy window. This will lead to lower numerical values of the attenuation coefficients, because more counts are acquired than is expected and this will be treated as less attenuation. Some type of correction for the downscatter is needed. Second, the source needs to be replaced more or less on an annual basis making the method relatively expensive. Third, the spatial resolution of the camera limits the details to the major structures, such as the lungs, so the attenuation map cannot be used as an anatomical reference map. In addition to these effects and dependent on the type of SPECT system, dead time problems and related mis-positioning of events can occur mainly in the daily collection of the blank scan than may affect the values in the map.

Commercial vendors have provided several types of transmission equipments based on radionuclides. Four principles are shown in Fig. 14.8. The most common solutions have been the use of a flood source (Fig. 14.8a) (either uncollimated or collimated), a scanning line source (Fig. 14.8b) and a fixed line source imaged with either a symmetrical fan-beam collimator (Fig. 14.8c) or an asymmetrical fan beam (Fig. 14.8d). A version of the geometry in Fig. 14.8a has been manufactured that rely on multiple replaceable line sources fixed in position such that the strongest of the line sources irradiates the thickest part of the patient where the photon attenuation dominates. The advantage is that as the line sources reduce in strength they can still be useful after reordering them. The solutions shown in Fig. 14.8c and d are found on triple-head SPECT system where one head is designated for the transmission measurement and utilizes special types of collimators. Furthermore, the dead time problems, caused by high count rates in regions of the crystal outside the patient boundary, can thereby be reduced.

The recent developments of combined SPECT/CT systems cancel most of the serious issues with radionuclide-based transmission measurements. The resolution and noise characteristics are superior and consequently, the quality of the measured attenuation coefficients is therefore high. The scaling to other photon energies is relatively accurate despite the fact that CT images are created from a broad spectrum of bremsstrahlung photon energies. The latest SPECT/CT models include diagnostic CT (spiral) with a very fast scanning time

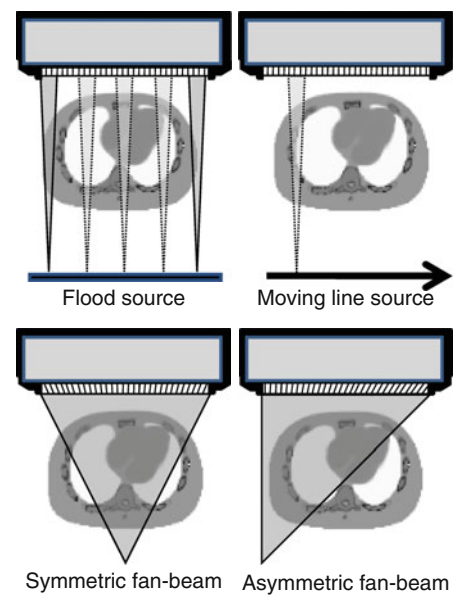

Fig. 14.8 Four common configurations for transmission measurements using a radionuclide source. The first is a fixed flood source; the second is a scanning line source. Third and fourth are fixed line sources together with a symmetrical (**c**) and an asymmetrical fan-beam collimator

and a spatial resolution that meets the requirement for a useful diagnostic modality in Radiology in contrast to the first-generation SPECT/CT system that had a spatial resolution of about 3 mm. However, care should be taken, since snaps shots from the CT does not generally represent the average attenuation caused by the breathing that is 'seen' by the SPECT camera. Artifacts can therefore be introduced in an attenuation correction. For more information on combined SPECT/CT system, see Chap. 10 in this textbook.

14.3.3 Scatter Correction Methods

Correction for scatter is most often made either in the energy domain where scatter in the photopeak energy window is modeled by collected data in additional energy windows or by using analytical methods that model the scatter on photopeak data directly. An early suggested scatter correction was the dual-energy window method (DEW), proposed by Jaszczak [10]. This method is based on an additional acquisition in a wide lower energy window. Scatter subtraction was applied by assuming that the distribution of counts in this lower energy window qualitatively equals to the distribution of scatter in the photopeak window but only differs quantitatively by a scaling factor k. A scatter-corrected projection is then calculated from

$$P(x,y)_{\text{Primary}} = P(x,y)_{\text{total}} - k \cdot P(x,y)_{\text{2nd}} \qquad (14.8)$$

The main problem with this method is to obtain a proper value of k since this factor is essentially a function of the patient geometry and source distribution. Furthermore, the distribution of scatter in the lower energy window include a larger fraction of events created from multiple-scattered photons with wide angles which may then cause either over- or undercorrections in specific regions even if the k factor is accurate.

A similar approach is used in the Triple-Energy Window (TEW) method, but this method is based on two narrow adjacent-located energy windows around the photopeak window [11]. By taking the average of the acquired images pixel-by-pixel and scale by the ratio between the energy window width of the photopeak window and the scatter windows a better scatter estimate will be obtained. Here, a scatter-corrected projection is obtained from

$$P(x,y)_{\text{Primary}} = P(x,y)_{\text{Peak}} - \left[\frac{P(x,y)_{\text{left}}}{\Delta E_{\text{left}}} + \frac{P(x,y)_{\text{right}}}{\Delta E_{\text{right}}}\right] \times \frac{\Delta E_{\text{Peak}}}{2} \qquad (14.9)$$

This method does not rely on any scaling factor. However, the main problem here is the noise in the scatter data that is mainly a result of the narrow energy windows (Fig. 14.9) and scatter images require further processing such as low-pass filtering before subtraction. Nevertheless, this method has been successful not only for ^{99m}Tc studies but also for ^{131}I studies where the upper scatter window take into account the down scatter from the 634 keV and 723 keV photons that are emitted in the ^{131}I decay.

Figure 14.10 shows simulated point-spread functions for different point-source locations in an 11 cm radius cylindrical water phantom. The unscattered primary component has been separated and is shown as dashed lines. The shape of the scatter component in a point-spread function very much depends on the source depth. For shallow source depths, the probability for multiple scattering is low and therefore the shape of the scatter profile is quite narrow. For large source depth, the distribution becomes wider because of more events from multiple-scattered photon that results in a registered position far away from the decay location.

A variety of methods are proposed based on analytical description of scatter point-spread function as an alternative to energy window-based methods. An early paper by Axelsson et al. [12] presented a convolution-subtraction method where a scatter point-spread function (spsf) was estimated by a single exponential function obtained by a line-fitting procedure of the tails in a measured point-spread function from a point source in a cylindrical phantom.

$$P(x,y)_{\text{Primary}} = P(x,y)_{\text{Peak}} - P(x,y)_{\text{Peak}} \otimes spsf \qquad (14.10)$$

The drawback with this method is that the scatter function is stationary and dependent on an estimated

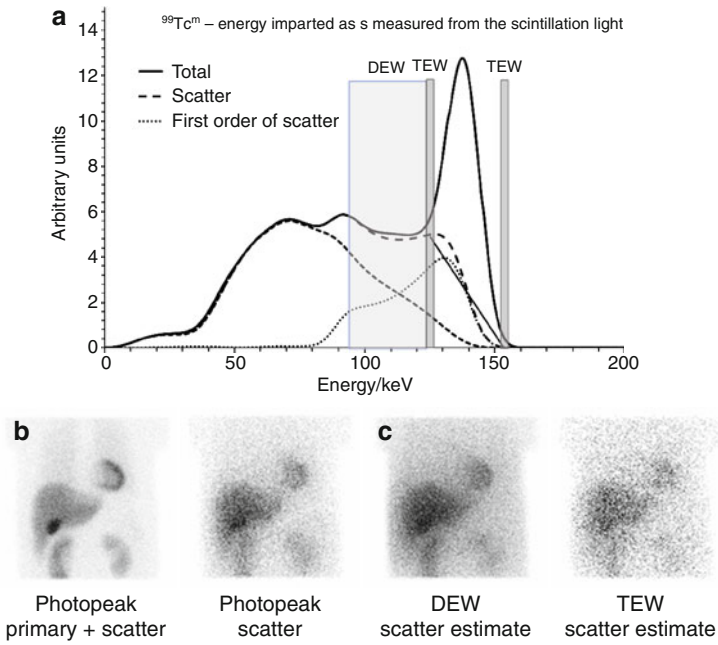

Fig. 14.9 The graph shows the location of the DEW window and the TEW windows. Image (**a**) shows the true scatter in the photon-peak energy window. Image (**b**) shows how this scatter distribution is estimated by a lower wider energy window (The DEW Method). Image (**c**) shows the scatter estimated by the TEW method where two narrow energy windows (width 4 keV) are positioned on each side of the main photon-peak window. The simulated spectrum has been divided into parts of total scatter, first order scatter, and second or more orders of scatter. It can be seen that more second or more orders of scattered event is recorded in the DEW region as compared to the photopeak region. This means that the distribution of scatter will be different in the DEW window, which will result in both over- and undercorrections when subtracting the data from the photopeak. The difference in distributions can be seen in the images. The problem of noise in the TEW windows due to the narrow energy window size is also evident

patient size and that the scatter close to the source is underestimated. A similar method based on a deconvolution process was investigated by Floyd [13]. Transmission-dependent scatter correction (TDSC) is an extension to the convolution-subtraction model in such a way that the scatter in the image is obtained by including a depth-dependent scatter function that scales the convolution kernel dependent on patient thickness. The fraction of scatter is used to scale the normalized convolving function before applying the convolution-subtraction process. The scatter fraction is determined from a generalized description of build-up functions for geometrical-mean images by Siegel et al. [14], where the buildup can be calculated as function of the depth for a given photon energy and composition

$$B(d) = a - b \cdot \mathrm{e}^{-\mu d\beta} \tag{14.11}$$

The scatter-to-total fraction [15] can then be derived.

$$\mathrm{SF} = 1 - \frac{1}{a - b(e^{-\mu T})^{\beta/2}} \tag{14.12}$$

and in the case of a transmission measurement

$$\mathrm{SF}(x,y) = 1 - \frac{1}{a - b\left(\frac{P(x,y)_{\mathrm{Patient}}}{P(x,y)_{\mathrm{Air}}}\right)^{\beta/2}} \tag{14.13}$$

where P_{patient} and P_{air} are projections with and without a patient in site, respectively. The constants a, b and needs to be determined by experimental measurements. By including a position-dependent *SF (x,y)* information, Equation 14.10 will be transformed into

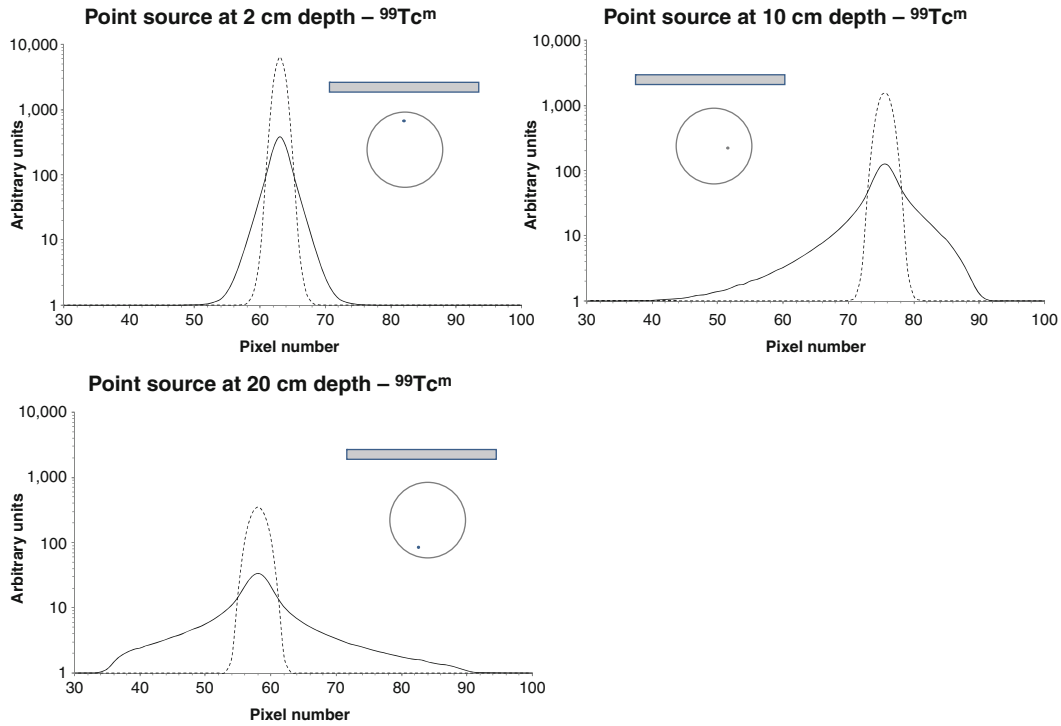

Fig. 14.10 Point-spread functions for three locations inside a cylindrical water phantom. The primary unscattered component is shown as *dashed lines*. Note the shade in distribution of the scatter as function of source depth. Also note also the nonsymmetry.

$$P(x,y)_{\text{Primary}} = P(x,y)_{\text{Peak}} - P(x,y)_{\text{Peak}} \otimes spsf \cdot SF(x,y) \tag{14.14}$$

An evaluation of the TDSC method using CT-based transmission data has recently been published by Willowson et al. [16]. Ljungberg and Strand [17, 18] further developed the convolution-subtraction method by use of Monte Carlo-calculated scatter line-spread functions tabulated as function of position in a cylindrical phantom. The scatter was estimated by selecting the scatter functions for each voxel that matched the voxel location as obtained from a reconstruction SPECT image.

Frey et al. [19] have developed a method called ESSE (Effective Scatter Source Estimator), in which the modeling of the scatter is incorporated in an iterative reconstruction method using precalculated scatter functions. The method has been proven to be useful and accurate for several radionuclides and also efficient when calculating the crosstalk of scatter between two energy windows [20]. However, the method has a limited accuracy in nonhomogeneous regions and in cases where activity out-of-field-of-view becomes important.

The most advanced and potentially accurate methods today are based on a real-time Monte Carlo calculation of the scatter. Floyd et al. pioneered this field already in the mid 80s, but because of limitations in computing resources the method did not reach a clinical practice [21]. However, today, it is possible to perform fast and accurate scatter modeling for an individual patient geometry and source distribution [22]. In these methods, the activity distribution at various steps in an iterative reconstruction process are linked to an external Monte Carlo-based forward projector that, based on the estimated activity distribution, calculates projection that fully include modeling of scatter in nonuniform regions. The method has been proven clinically useful mainly because of the implementation of fast variance reduction methods especially when modeling the collimator response, and studies have been made for ^{99m}Tc [23, 24] and ^{201}Tl [25]. This method can also include compensation

for septum penetration in the collimator and back scatter for components behind the crystal and can therefore be useful for ^{131}I studies [26]

14.3.4 Spatial Resolution Compensation Methods

Compensation for the degradation in spatial resolution due to the collimator-response function (CRF) improves spatial resolution and provides improved quantitative accuracy for small objects. There are two classes of methods: iterative and noniterative methods. Noniterative methods include restoration filters, such as Metz and Wiener filters [27]. These filters are generally applied in the frequency domain and the usage is to filter the image data with a spatially invariant filter that described the inverse of the PSF function. They will, however, not be as effective at removing spatial varying effects as compared to iterative methods and they tend to have poor noise properties since the inverse filters generally act as a high-pass filter amplifying noise.

Some of the noniterative methods are based on the frequency distance relation (FDR) that relates the position of a source to the Fourier transform of the corresponding sinogram of the source. For a distributed source, measured activity from all sources located at the same distance from the center of rotation appears along a single line in Fourier space. One can therefore use this information in an inverse filtering method along these lines with a properly selected CRF [28,29].

In an iterative reconstruction method, the spatial resolution can be partly compensated for by including a model for distance-dependent blurring in the projector steps (forward and backward). This means that instead of forwarding the data in straight lines along the columns when calculating the projection value, the projector include the probability for a photon to pass nearby holes. This spread is often described by a distance-dependent spatially invariant Gaussian function, but images of the point-spread function can also be explicitly calculated and stored for each distance by Monte Carlo simulation for those cases where septum penetration is important (i.e., imaging with ^{131}I and ^{123}I radiopharmaceuticals). The correction method has an effect similar to low-pass filtering, but it is not perfect in that sense that it will restore perfect resolution since some information about high spatial frequencies is permanently lost. Iterative reconstruction CRF compensation also produces different noise patterns as compared to filtered backprojection methods or iterative reconstruction without CRF correction. The correction method tends to increase the noise in the middle frequency range that may result in a blobby pattern in the reconstructed images, but noise properties can be improved by accurate modeling of CRF [30]. Some recent software programs are written to shorten acquisition time by incorporating the resolution recovery into the reconstruction process. This helps to improve the resolution properties of the image and hence signal-to-noise ratios for data acquired with less count statistics [31].

The degradation of spatial resolution is a function of the distance from the face of the collimator. Thus, a prerequisite to model CRF is the information of the distance from the center of rotation to the collimator face for every acquisition angle along with the knowledge of the collimator characteristics. For systems using circular orbits, this information is defined by the radius of rotation. For state-of-the-art SPECT system, the distance between the camera and the patient can, for each angle, be fine-tuned by sensors on the scintillation camera head. If this method is used, then a CRF correction requires the information of the varying organ-to-collimator distances for a particular projection angle. This information, however, is not always available from commercial systems or file headers.

14.3.5 Partial Volume Correction

Reconstructed SPECT images obtained by filtered backprojection or iterative reconstruction are degraded by the limited spatial resolution of the collimator system resulting in significant partial volume effects (Fig. 14.11). Because of this effect, spill-in of counts can be significant when evaluating activity in small regions located in close proximity to neighboring objects with high activity uptake. In a similar way, spill-out occurs when quantifying high activity and activity concentrations in small regions. In these cases,

it might therefore be of importance to include some kind of partial volume correction (PVC).

Partial volume effects are of particular interest in clinical applications, e.g., determination of myocardial wall thickness, in quantitative brain studies where activity concentrations in small structures will be underestimated, and in dosimetry for radionuclide therapy where uptake by small tumors may be important for accurate dose assessment.

The underlying assumption for most PVC methods is that the radioactivity uptake in a specific volume is uniformly distributed and that the change in counts in this volume therefore can be used to develop a correction method. In the past, correction factors (recovery coefficients) for partial volume effects have been determined based on measurements of spheres of various sizes in physical phantoms [32–34]. The accuracy of these correction methods is, however, highly dependent on the shape of the tumor and on the background activity of the target structure. A more general approach is to minimize the resolution and penetration effects by implementing a 3D depth-dependent detector response included into the system model of an iterative reconstruction. These implementations have resulted in improved quantification accuracy for higher energy photon emitters such as ^{111}In and ^{131}I [35–37]. However, these studies show that for small targets and for targets within a high background activity, the activity recovery is not complete even when a 3D depth-dependent detector response function is included in the system model.

With the recent availability of dual modality SPECT-CT imaging with good image registration there is much incentive to use the CT-based anatomical information to correct for partial volume effects. CT-defined templates have been used for SPECT partial volume correction in myocardial studies [38] in which user-defined templates were mathematically projected to mimic the SPECT process followed by an image reconstruction to obtain a pixel-by-pixel PVC for the myocardial region. In more recent SPECT studies, the original template-based PVC was modified to implement a perturbation-based template method, which accounts for the nonlinear effects of the iterative reconstruction [37, 39, 40]. With this, PVC-improved quantitative accuracy has been demonstrated for SPECT studies with both ^{99m}Tc, ^{111}In and ^{131}I.

The method works as follows: Separate templates are generated for each target and relevant background structure by defining volume-of-interest (VIO) outlines in three dimensions on the registered anatomical

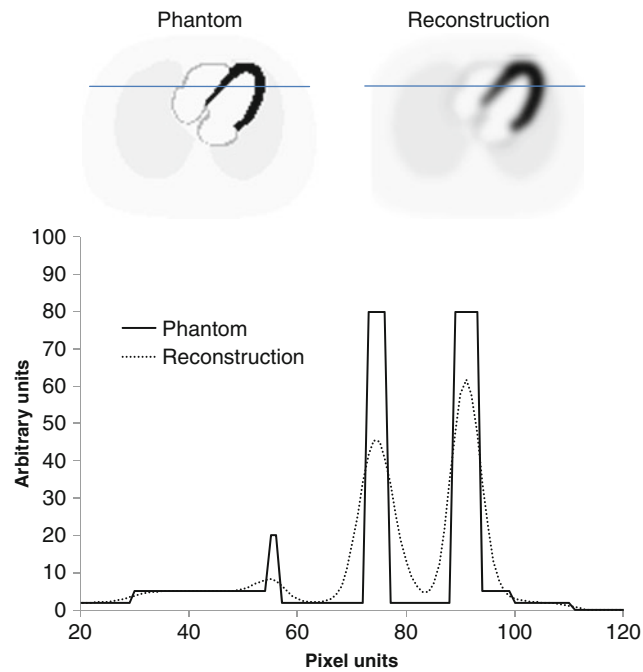

Fig. 14.11 The figure shows the effect of partial volume. The *left image* shows the real activity distribution ("phantom") and the *right figure* shows the image blurred by a Gaussian function that simulate a LEHR collimator and a clinically realistic source-to-collimator distance. The profiles through the heart show the "spill-in" into the left ventricle and "spill-out" from the myocardial region

CT image. All voxels located within the template are assigned a value of unity. Each template is then independently projected into appropriate number of angular views using an analytical (or Monte Carlo based) projector, which realistically model the SPECT imaging process. The next step is to reconstruct the reprojected template SPECT projections to transversal images of pixel-by-pixel correction factors for the VOIs in the SPECT image. Figure 14.12 shows a block diagram showing the steps for template generation, forward projection, image reconstruction and the PVC.

When reconstructing the template projections one needs to account for the nonlinearity of the iterative reconstruction algorithm. This can be done as proposed by Boening et al. [40] and Yong et al. [39], where each template is introduced as a small perturbation to the emission data set. For each of the target and background VOI defined in the image, a reconstructed template T is calculated to carry out the spill-in and spill-out correction for each of the regions defined in the image. The correction for spill-in of counts from background to target is given by

$$C_{SI}(X_j) = X_j - \sum_n T_{j,n}^{bkg} \cdot a_n \qquad (14.15)$$

where $C_{SI}(X_j)$ is the spill-in-corrected image at pixel j, X_j is the uncorrected image at pixel j, $T_{j,n}$ is the reconstructed template at pixel j for the nth background region and a_n is the average count in the uncorrected image for the nth background region. Note that nontarget regions are treated as background regions that may potentially contribute spill-in counts into the target. The PVC completes by applying the spill-out correction to the spill-in-corrected image

$$C_{SO+SI}(X_j) = \frac{C_{SI}(X_j)}{T_j^{tgt}} \qquad (14.16)$$

where $C_{SO+SI}(X_j)$ is the spill-out and spill-in-corrected image at pixel j and $T^{tgt}{}_j$ is the reconstructed target template at pixel j. In patient imaging, separately defining templates for all of the background structures may not be practical since it may take a larger amount of time. A practical alternative would be to define templates for the targets and combine all of the other regions to form one background template, assuming uniform activity in this region .

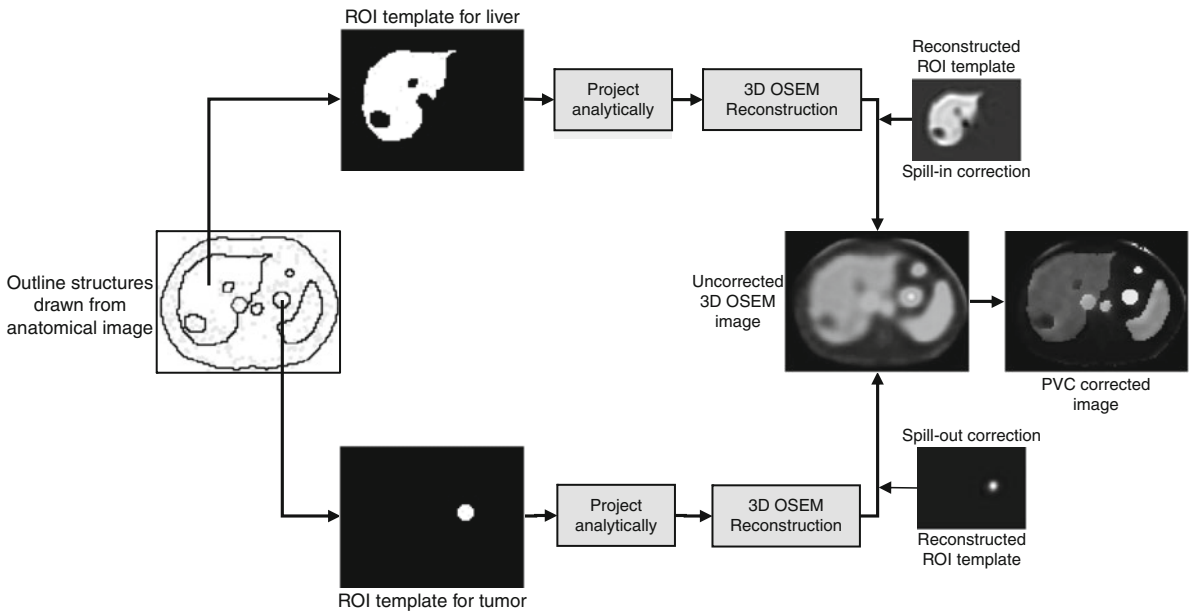

Fig. 14.12 The flowchart shows the principle steps in an image-based partial–volume correction. The user draws templates of the outline of the target (in this case a tumor) and relevant background regions from a high-resolution anatomical image. The values of each pixel in the ROIs are assigned unity. An analytical projection including simulation of distance-dependent collimator blur is then used to create projections of the templates. These projections are then reconstructed using the same reconstruction method as for the emission images. The reconstructed template images are then used to correct for the spill-in and spill-out

14.3.6 Influence of Correction Algorithms on Image Quality

Figure 14.13 shows some important factors and methods necessary to include in an quantitation procedure for SPECT. Photon attenuation is the single largest factor that degrades image quality in SPECT. Without proper compensation for attenuation, an absolute estimate of activity will often be in error by>50%. The magnitude of the effect is higher for low-energy photons and for large parts of the body with high density. Nonuniform attenuation in the head or the thorax can cause undesirable artifacts that impede both visual interpretation and activity quantitation.

Energy window-based scatter correction methods can be applied in two ways, either prior to reconstruction by simply subtracting the estimated scatter from the projection data prior to reconstruction or incorporating the scatter estimate in an iterative reconstruction method. The disadvantage of the first approach is the fact that subtracting two noise images results in an increase of the noise. This means that some kind of low-pass filtering may be necessary to apply on the data resulting in a degradation of the spatial resolution of the image. The second approach of incorporating the measured scatter estimate in the forward projection has shown to have better noise properties but may be technically more complicated to implement. Further, accurate scatter correction techniques should improve image contrast and lead to a better quantitative accuracy.

The necessity for quantitative SPECT images depends on the application. It is, however, important to understand that even if the actual number in units of MBq or MBq/mL is not used for a particular application, the quantification procedures may improve the accuracy and precision in the investigation since compensations correct for the mis-placement of counts and thus provide a better image. On the other hand, if the correction methods used are not properly setup and

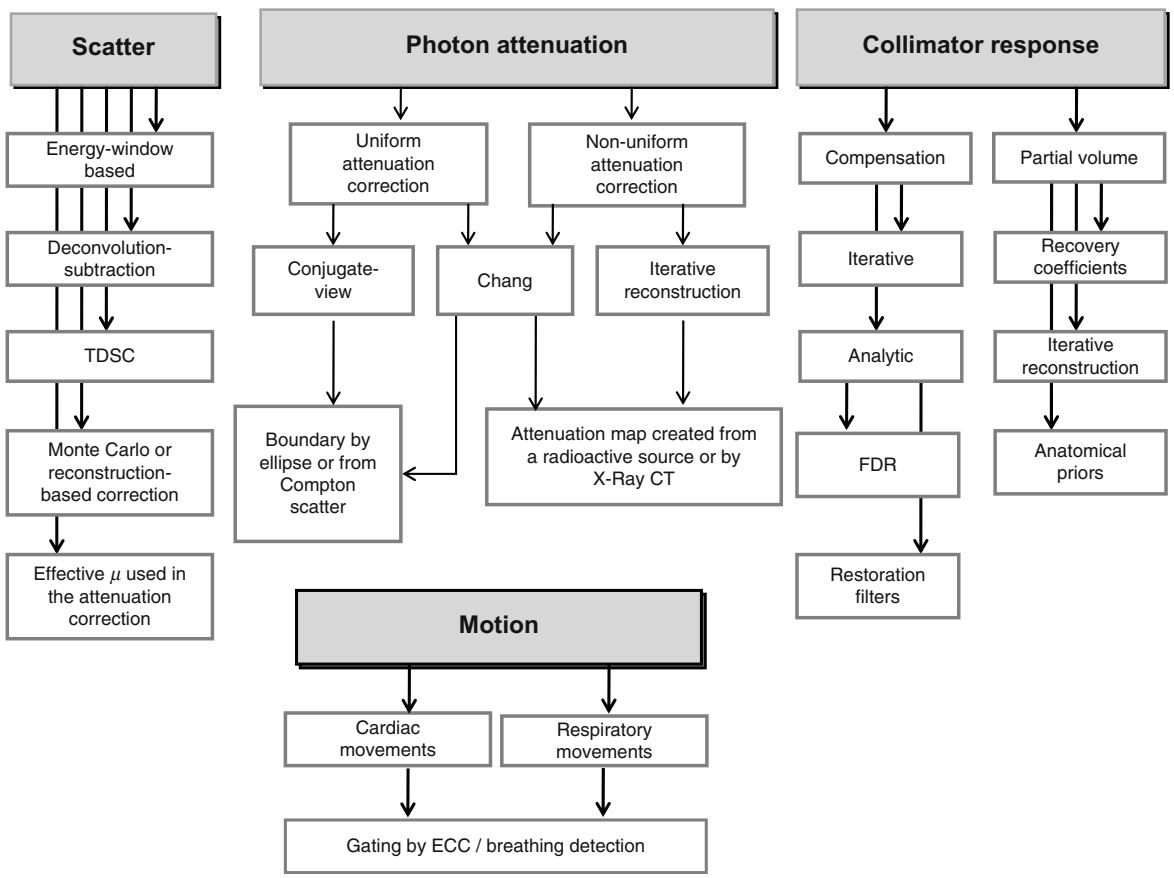

Fig. 14.13 This flowchart summarizes the different factors that are necessary to consider when performing quantitative SPECT

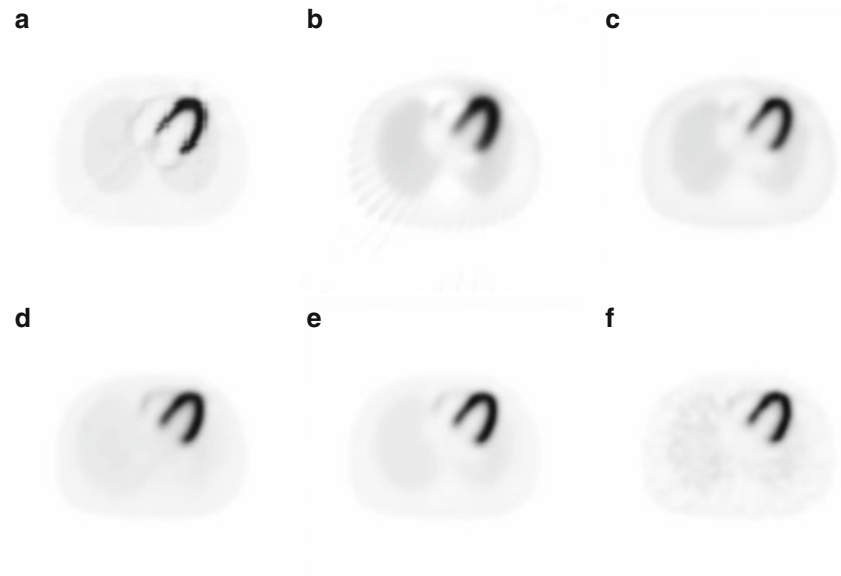

Fig. 14.14 The first image (**a**) is reconstructed data mimicking a perfect system without patient movements (the image is equal to Fig 14.7a). The second image (**b**) shows an image of the same data set reconstructed with filtered backprojection without corrections. Figure (**c**)–(**e**) shows images reconstructed with OSEM (6 iterations and 16 subsets) using nonhomogeneous attenuation correction (**c**), attenuation and scatter correction using the ESSE method (**d**), and scatter and attenuation correction together with CRF correction (**e**). (**f**) shows an image reconstructed with all correction methods but using a data set with a realistic noise level added

validated then this can lead to problems. Furthermore, in some cases, image noise can be amplified which is a degrading factor on the image quality despite the theoretical improvement due to a particular compensation.

Despite the many inherent problems with SPECT images, the recent advancement in developing correction methods for physical effects, such as photon attenuation, scatter and collimator resolution has made SPECT a quantitative tool for activity measurement. Figure 14.14 shows an example of state-of-the-art reconstruction and activity quantification method including nonuniform attenuation correction, scatter correction using the ESSE method [41] and spatial variant collimator response correction.

14.4 Applications of SPECT in Dosimetry

One of the areas in nuclear medicine applications that rely on the absolute values of the SPECT images is dosimetry in radionuclide therapy where multiple SPECT acquisitions form the base for a dose planning of the therapy. The absorbed dose is defined as the imparted energy dE within a volume of interest divided by the mass of the volume element dm or D=dE/dm (1 Gy=1 J/kg). In practice, the absorbed dose is average over a large volume than dm, which yields $D = \bar{E}/m$. Dosimetry with quantitative SPECT allows for absorbed dose estimation within an organ down to a voxel level.

14.4.1 The Basic Calculation Scheme

The basic equation for dose calculations has been given by a MIRD publication [42] and is described as

$$\int \dot{D}(t)\,\mathrm{d}t = \tilde{A} \cdot S = \int A(t)\mathrm{d}t \cdot \frac{n_i E_i \varphi_i(k \leftarrow h)}{m} \qquad (14.17)$$

where n is the number of particles i per disintegration, E_i is the average energy emitted for particle i, is a geometrically related factor that describes the fraction of energy emitted from a source volume element h that is absorbed in a target volume element k. Finally, m is

the mass of that target volume element. The right integral is the cumulative activity i.e., the total number of disintegrations during a time interval from time of injection to infinity (see Chap. 8 for further details).

In practice, the integral (or the area under the curve) is mostly determined by a curve-fitting procedure from a limited number of time-activity values as have been measured by a scintillation camera or SPECT. The cumulative activity then equals the area under the curve and if expressed per unit administered activity is called the residence time. Recently, He and colleagues [43] have investigated several methods to determine the residence time including both commonly used quantification planar protocols as well as quantitative SPECT and a combined hybrid method. The latter is based on defining VOIs of the major organs in a patient from a CT study and with an iterativeMLEM method including a forward projector adjusting the activity in the VOIs to match the measured data [44]. This method has shown to be more accurate than conventional planar methods but has practical limitations in the time required for defining the VOI in 3D (mainly manual segmentation).

The estimation of risks for developing cancer due to the usage of radiation is calculated using precalculated S values that have been developed by Monte Carlo calculations for generic mathematical description of a population of interest. This is because such risk estimations are relevant only on a large population of individuals. Therefore, such mathematical descriptions represent a reference male or female i.e., an average of a large population. These S values tables have been compiled in terms of the absorbed dose (Gy) to the target volume per cumulative activity (MBqh) in the source organ. S values are embedded into useful programs, such as, the MIRDDOSE3 [45] and the newly developed OLINDA code [46]. However, the mathematical phantoms have not been developed for individual therapy planning and therefore the dose-conversion factors are not very well representative for a specific patient. To overcome this, one may need to implement the patient's own geometry and biokinetics into a dose calculation scheme. A principal flowchart showing the steps necessary to consider for 3D patient-specific SPECT (and PET) dosimetry is shown in Fig. 14.15.

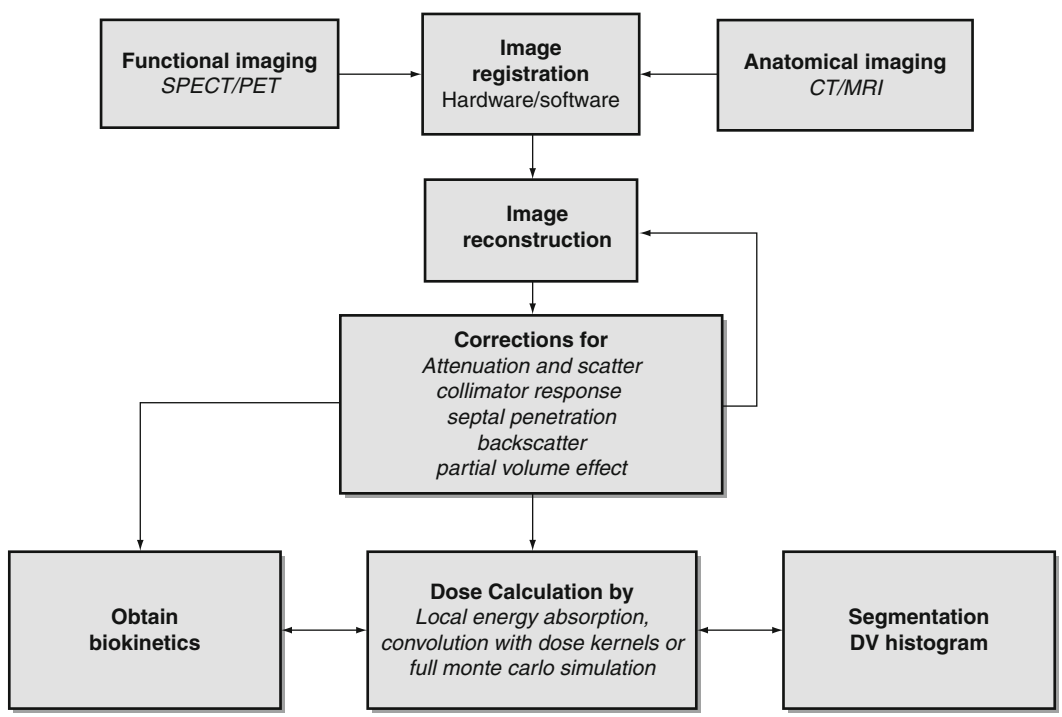

Fig. 14.15 A flowchart describing the different steps toward a dosimetry calculation based on quantitative SPECT images

14.4.2 Dose Calculation from Quantitative SPECT Imaging

Most dosimetry studies with scintillation cameras are conducted by planar scintillation camera imaging using the conjugate-view method. As described earlier, this method relies on opposite projections, and if the geometrical mean of the opposite projection is taken, the dependence on the source depth is greatly reduced. The attenuation correction then depends only on the "thickness of the patient" because the attenuation depend on the whole patient geometry and not on the source location. This is the idea behind the geometrical-mean method. First, the above statement is valid only for a point source. If extended sources are being imaged (which is always the case in clinical studies), then a correction for the source thickness needs to be made [47]. Second, if over- and underlying activities are present, this affects the quantitation, since the planar imaging is on a 2D modality and corrections needs to be made [48]. Third, scatter correction and septum penetration may not be accurately modeled and fourth, the dosimetry needs in most cases to rely on S-factors obtained from a mathematical phantom.

SPECT in combination with CT can overcome many of these drawbacks because of the inherent 3D activity determination. The methods, described below, treat each voxel as a source volume and correspondingly each voxel as a target organ. In practice, one does not store the *S*-factor that corresponds to each combination but the MIRD Equation 14.17 will remain valid in these cases. The results will be 3D images of absorbed dose distributions useful to obtain, for example, dose-volume histograms and other parameters related to the heterogeneity of imparted energy within the volume of interest.

14.4.3 Energy Locally Absorbed within a Voxel

In its simplest form, a dose calculation based on quantitative SPECT can assume all kinetic electron energy emitted from the radionuclide as locally absorbed within the voxel volume and disregard the energy distribution from photons. The absorbed dose is then calculated from the mass of the volume element. This assumption is not as approximate as it sounds because the spatial resolution of a SPECT image used as input is in the same order or larger compared to relevant electron ranges. Thus, the SPECT image may very well show the absorbed dose distribution from electrons. If reviewing Equation 14.17 above, this method corresponds to the case where source volume equals the target volume ($k=h$). This type of calculation may work only on pure emitting radionuclides such as ^{90}Y or when the contribution to the absorbed dose from photons can be regarded as negligible.

14.4.4 Convolution Based on Point Dose Kernels

This method use precalculated energy distribution in 3D from a point source usually stored as function of the radial distance from the point source normalized to the energy emitted per disintegration. By a mathematical convolution either in the spatial domain or in the frequency domain, the initial activity image (e.g., a SPECT image) can be converted to absorbed dose images. Berger has published point dose kernel for both photons [49] and electrons and particles [50]. Convolution of SPECT images with point-dose kernels should generally be used when the voxel size of the activity matrix is small as compared to the path length of the particles. Also note that dose kernels generally are valid for a uniform material (often water or tissue-equivalent material) and that the calculation procedure (often performed in the Fourier domain) is spatially invariant and do not take into account variations either in density or changes in energy distribution due to organ or patient boundaries. An example of a program for dosimetry that uses point dose kernels is the 3D-ID program [51].

14.4.5 Full Monte Carlo Simulation

The most accurate absorbed dose calculation, but also the most complex and computing demanding procedure, is a full radiation transport calculation using the Monte Carlo method [52]. The method in this context

starts from quantitative accurate SPECT images and registered density images, usually obtained from a patient-specific CT. From this set of images, simulation of individual photon and electron interactions are performed in the 3D density volume by tracing the particles to the end by explicitly simulating all relevant interaction types. The location for a decay corresponds to the apparent voxel location in the Cartesian coordinate system and the numbers of simulated decays are proportional to the voxel values of the quantitative SPECT images. The imparted energy from each particle is then scored in a matching 3D-absorbed energy matrix as the particles are traced through the volume. When all particles are simulated, the absorbed energy in each voxel per voxel mass obtains the absorbed dose. The main advantage with full Monte Carlo simulation is that it considers the patient's geometry and that heterogeneities in density and tissue compositions can be included in the absorbed dose calculation.

There are several very competent programs in the public domain that is useful for Monte Carlo absorbed dose calculations. The EGS family of programs [53] have shown to be useful and simulation of voxel data is relatively straight forward – although the program required some programming skills. MCNP is also a program that can implement voxel information [54]. In Medical Imaging applications, the GATE Monte Carlo program [55] has gained increased interest due to its flexibility especially with complex geometries. This program is a layer of the Geant4 program from CERN and can simulate charged particles up to very high energies.

14.4.6 Considerations Related to Absorbed Dose Calculation Based on SPECT/CT Data

The new hybrid systems offer a good possibility to do accurate dosimetry both in 2D and in 3D. Today, most SPECT/CT systems are based on diagnostic CT acquisition with a spatial resolution of the order of a magnitude higher that SPECT unit. In some systems, the CT unit is useful to obtain information about the attenuation for the planar conjugate-view method by performing a full-length scan (so called scout measurement). If the scaling between pixel units and density can be determined, then this transmission image will be the correction necessary for planar attenuation correction [56]. The high quality from diagnostic CT units makes accurate SPECT quantification possible and the known limitations with radionuclide-based transmission sources (down scatter, noise and limited spatial resolution) is eliminated by using CT.

Some issues needs consideration when doing absorbed dose calculations based on SPECT data. The most important is the fact that the SPECT images do not show the actual activity distribution. The images are affected by the particular system degradation in spatial resolution and the effect (discussed above in the partial volume section) is dependent on the source volume.

When calculating the absorbed dose, it is convenient to use the CT images if proper scaling to density can be achieved. However, in most modern system, the spatial resolution of the CT data can be in the order of a magnitude better then the SPECT information. When using high-resolution CT as mass images in the voxel-by-voxel absorbed dose calculation artifacts can be introduced where 'counts' spill out in regions of low densities. In addition, gas in the abdominal parts can result in very high absorbed doses because of low CT voxel values in combination with the blurring due to the limited spatial resolution in the SPECT images. One way to overcome this problem is to reduce the spatial resolution of the CT images by a convolution with a PSF that match the resolution of the SPECT system.

Most CT units are very fast in the image acquisition. This means that a CT image over the thorax may reflect a particular time segment of the breathing cycle more. A SPECT projection is generally acquired over a much longer time meaning that the image reflects a count distribution averaged over the whole respiration cycle. This can thus introduce artifacts in the attenuation correction and the absorbed dose calculations especially close to the lung boundaries.

Even if SPECT/CT images are accurately registered to each other in a hybrid system, there is a need for image registration when performing multiple SPECT/CT studies in order to obtain voxel-based time-activity curves. Image registration using CT-CT images are preferable here compared to SPECT-SPECT registration because of their better similarity. However, if a diagnostic CT is used, then the absorbed dose caused by multiple X-rays exposures can be significant. The problem can be reduced if the CT unit can be run in a 'low-dose' mode. The signal-to-noise ratio and spatial resolution may be reduced here, but for attenuation

corrections and absorbed dose calculations, this is probably not a serious problem.

14.5 Conclusion

Today, quantitative SPECT has become a reality mainly because of the great improvement in reconstruction algorithms where the corrections for image degradation due to photon attenuation, contribution of event in the image from photons scatter in the patient, collimator and camera housing and septum penetration can be made in a consistent and natural way in the forward projector step. The limitations that existed in earlier radionuclide-based transmission measurement methods are eliminated when using high-quality attenuation maps created by CT detectors that are integrated into the SPECT gantry. Hybrid SPCT/CT systems also provide registered functional and anatomical images thus reducing the need for software registration methods, although good registration software may be required when working with multiple SPECT/CT studies. Many scatter correction methods still rely on measurements in secondary energy window, but along with the improvement in computing power, real time Monte Carlo simulation of scatter may be feasible clinically within a few years.

References

1. Ljungberg M, Strand SE (1989) A Monte Carlo program simulating scintillation camera imaging. Comput Meth Prog Bio 29:257–272
2. Ljungberg M (1998) The SIMIND Monte Carlo program. In: Ljungberg M, Strand SE, King MA (eds) Monte Carlo calculation in nuclear medicine: applications in diagnostic imaginged. IOP, Bristol/Philadelphia, pp 145–163
3. Segars WP, Lalush DS, Tsui BMW (1999) A realistic spline-based dynamic heart phantom. IEEE Trans Nucl Sci 46(3):503–506
4. Segars WP (2001) Development of a new dynamic NURBS-based cardiac-torso (NCAT) phantom. PhD Thesis, Universiy of North Carolina
5. Berger MJ, Hubbell JH (1987) XCOM: Photon Cross Sections on a Personal Computer, NBSIR 87–3597, National Bureau of Standards (former name of NIST), Gaithersburg, MD, http://physics.nist.gov/PhysRefData/Xcom/Text/version.shtml
6. Dewaraja YK, Ljungberg M, Koral KF (2000) Characterization of scatter and penetration using Monte Carlo simulation in 131-I imaging. J Nucl Med 41(1):123–130
7. Dewaraja YK, Ljungberg M, Koral KF (2000) Accuracy of 131I tumor quantification in radioimmunotherapy using SPECT imaging with an ultra-high-energy collimator: Monte Carlo study. J Nucl Med 41(10):1760–1767
8. Slomka PJ, Nishina H, Berman DS et al (2004) "Motion-frozen" display and quantification of myocardial perfusion. J Nucl Med 45(7):1128–1134
9. Chang LT (1978) A method for attenuation correction in radionuclide computed tomography. IEEE Trans Nucl Sci 25:638–643
10. Jaszczak RJ, Greer KL, Floyd CE et al (1984) Improved SPECT quantification using compensation for scattered photons. J Nucl Med 25:893–900
11. Ogawa K, Harata H, Ichihara T et al (1991) A practical method for position dependent compton-scatter correction in single photon emission CT. IEEE Trans Med Imaging 10:408–412
12. Axelsson B, Msaki P, Israelsson A (1984) Subtraction of compton-scattered photons in single-photon emission computed tomography. J Nucl Med 25:490–494
13. Floyd CE, Jaszczak RJ, Greer KL et al (1985) Deconvolution of compton scatter in SPECT. J Nucl Med 26:403–408
14. Siegel JA, Wu RK, Maurer AH (1985) The buildup factor: effect on scatter on absolute volume determination. J Nucl Med 26:390–394
15. Meikle SR, Hutton BF, Bailey DL (1994) A transmission-dependent method for scatter correction in SPECT. J Nucl Med 35:360–367
16. Willowson K, Bailey DL, Baldock C (2008) Quantitative SPECT reconstruction using CT-derived corrections. Phys Med Biol 53(12):3099–3112
17. Ljungberg M, Strand SE (1990) Scatter and attenuation correction in SPECT using density maps and Monte Carlo simulated scatter functions. J Nucl Med 31:1559–1567
18. Ljungberg M, Strand SE (1991) Attenuation and scatter correction in SPECT for sources in a nonhomogeneous object: a Monte Carlo study. J Nucl Med 32:1278–1284
19. Frey EC, Tsui BMW (1997) A new method for modeling the spatially-variant, object-dependent scatter response function in SPECT. In: Conference records of the IEEE Medical Imaging Conference, Anaheim, 1996, pp 1082–1082
20. Song X, Frey EC, Wang WT et al (2004) Validation and evaluation of model-based crosstalk compensation method in simultaneous 99mTc Stress and 201Tl rest myocardial perfusion SPECT. IEEE Trans Nucl Sci 51(1):72–79
21. Floyd CE, Jaszczak RJ, Coleman M (1985) Inverse Monte Carlo: a unified reconstruction algorithm for SPECT. IEEE Trans Nucl Sci 32:779–785
22. Beekman FJ, de Jong HW, Slijpen ET (1999) Efficient SPECT scatter calculation in non-uniform media using correlated Monte Carlo simulation. Phys Med Biol 44(8): N183–N192
23. Xiao J, de Wit TC, Staelens SG et al (2006) Evaluation of 3D Monte Carlo-based scatter correction for 99mTc cardiac perfusion SPECT. J Nucl Med 47(10):1662–1669
24. Liu S, King MA, Brill AB (2008) Accelerated SPECT Monte Carlo simulation using multiple projection sampling

and convolution-based forced detection. IEEE Trans Nucl Sci 55(1):560–568
25. Xiao J, de Wit TC, Zbijewski W et al (2007) Evaluation of 3D Monte Carlo-based scatter correction for 201Tl cardiac perfusion SPECT. J Nucl Med 48(4):637–644
26. Shaoying L, King MA, Brill AB et al (2008) Convolution-based forced detection Monte Carlo simulation incorporating septal penetration modeling. IEEE Trans Nucl Sci 55(3): 967–974
27. King MA, Schwinger RB, Doherty PW et al (1984) Two-dimensional filtering of SPECT images using the Metz and Wiener filters. J Nucl Med 25:1234–1240
28. Lewitt RM, Edholm PR, Xia W (1989) Fourier method for correction of depth dependent collimator blurring. Proc SPIE 1092:232–243
29. Xia W, Lewitt RM, Edholm PR (1995) Fourier correction for spatially variant collimator blurring in SPECT. IEEE Trans Med Imaging 14(1):100–115
30. Beekman FJ, Slijpen ET, de Jong HW et al (1999) Estimation of the depth-dependent component of the point spread function of SPECT. Med Phys 26(11):2311–2322
31. Borges-Neto S, Pagnanelli RA, Shaw LK et al (2007) Clinical results of a novel wide beam reconstruction method for shortening scan time of Tc-99m cardiac SPECT perfusion studies. J Nucl Cardiol 14(4):555–565
32. Zito F, Gilardi MC, Magnani P et al (1996) Single-photon emission tomographic quantification in spherical objects: effects of object size and background. Eur J Nucl Med Mol Imaging 23(3):263–271
33. Koral KF, Dewaraja Y (1999) I-131 SPECT activity recovery coefficients with implicit or triple-energy-window scatter correction. Nucl Instrum Methods Phys Res Sect A 422 (1–3):688–692
34. Geworski L, Knoop BO, de Cabrejas ML et al (2000) Recovery correction for quantitation in emission tomography: a feasibility study. Eur J Nucl Med Mol Imaging 27 (2):161–169
35. Dewaraja YK, Wilderman SJ, Ljungberg M et al (2005) Accurate dosimetry in 131I radionuclide therapy using patient-specific, 3-dimensional methods for SPECT reconstruction and absorbed dose calculation. J Nucl Med 46 (5):840–849
36. Ljungberg M, Sjogreen K, Liu X et al (2002) A 3-dimensional absorbed dose calculation method based on quantitative SPECT for radionuclide therapy: evaluation for 131-I using Monte Carlo simulation. J Nucl Med 43(8): 1101–1109
37. He B, Du Y, Song X et al (2005) A Monte Carlo and physical phantom evaluation of quantitative In-111 SPECT. Phys Med Biol 50(17):4169–4185
38. Da Silva AJ, Tang HR, Wong KH et al (2001) Absolute quantification of regional myocardial uptake of 99mTc-Sestamibi with SPECT: experimental validation in a Porcine model. J Nucl Med 42(5):772–779
39. Yong D, Tsui BMW, Frey EC (2005) Partial volume effect compensation for quantitative brain SPECT imaging. IEEE Trans Med Imaging 24(8):969–976
40. Boening G, Pretorius PH, King MA (2006) Study of relative quantification of Tc-99 m with partial volume effect and spillover correction for SPECT oncology imaging. IEEE Trans Nucl Sci 53 (3-part-2):1205–1212
41. Frey EC, Tsui BMW (1993) Modeling the scatter response function in inhomogeneous scattering media. In: Conference Records of the IEEE Medical Imaging Conference, pp 1–1
42. Loevinger R, Berman M (1976) A revised schema for calculation of the absorbed dose from biologically distributed radionuclides. MIRD Phamplet No. 1, Revised. Society of Nuclear Medicine, New York
43. He B, Wahl RL, Du Y et al (2008) Comparison of residence time estimation methods for radioimmunotherapy dosimetry and treatment planning–Monte Carlo simulation studies. IEEE Trans Med Imaging 27(4):521–530
44. He B, Frey EC (2006) Comparison of conventional, model-based quantitative planar, and quantitative SPECT image processing methods for organ activity estimation using In-111 agents. Phys Med Biol 51(16):3967–3981
45. Stabin MG (1996) MIRDOSE: personal computer software for internal dose assessment in nuclear medicine. J Nucl Med 37(3):538–546
46. Stabin MG, Sparks RB, Crowe E (2005) OLINDA/EXM: the second-generation personal computer software for internal dose assessment in nuclear medicine. J Nucl Med 46 (6):1023–1027
47. Fleming JS (1979) A technique for the absolute measurement of activity using a gamma camera and computer. Phys Med Biol 24(1):178–180
48. Sjögreen K, Ljungberg M, Strand SE (2002) An activity quantification method based on registration of CT and whole-body scintillation camera images, with application to 131I. J Nucl Med 43(7):972–982
49. Berger MJ (1968) Energy deposition in water by photons from point isotropic sources: MIRD Pamphlet no. 2. J Nucl Med 9:15–25
50. Berger MJ (1971) Distribution of absorbed dose around point sources of electrons and beta particles in water and other media: MIRD Pamphlet no. 7. J Nucl Med 12:5–23
51. Kolbert KS, Sgouros G, Scott AM et al (1997) Implementation and evaluation of patient-specific three- dimensional internal dosimetry. J Nucl Med 38(2):301–308
52. Andreo P (1991) Monte Carlo techniques in medical radiation physics. Phys Med Biol 36:861–920
53. Nelson WR, Hirayama H, Rogers DWO (1985) The EGS4 Code System. Stanford Linear Accelerator Center report SLAC-265
54. Briesemeister JF (1986) MCNP-A general Monte Carlo Code for Neutron and Photon Transport Version 3A, Los Alamos National Laboratory LA-7396-M. Online document at: http://mcnp-green.lanl.gov/index.html
55. Jan S, Santin G, Strul D et al (2004) GATE: a simulation toolkit for PET and SPECT. Phys Med Biol 49(19): 4543–4561
56. Minarik D, Sjögreen K, Ljungberg M (2005) A new method to obtain transmission images for planar whole-body activity quantification. Cancer Biother Radiopharm 20(1):72–76